X-ray analysis of temperature induced defect structures in boron implanted silicon

M. Sztucki[a,b)], T. H. Metzger[b)], I. Kegel[a)], A. Tilke[a)]

[a)] *CeNS at Ludwig-Maximilians-Universität München, Geschwister-Scholl-Platz 1, 80539 München, Germany*

[b)] *European Synchrotron Radiation Facility, BP 220, 38043 Grenoble Cedex, France*

J. L. Rouvière

CEA-Grenoble, Département de Recherche Fondamentale sur la Matière Condensée, SP2M, 17 rue des Martyrs, 38054 Grenoble Cedex 9, France

D. Lübbert[c,*)], J. Arthur[c)], J. R. Patel[c,d)]

[c)] *SSRL/SLAC, Stanford University, Stanford, CA 94309, USA*

[*)] *Present address: HASYLAB/DESY, Notkestr. 85, 22603 Hamburg, Germany*

[d)] *ALS/LBL, 1 Cyclotron Road, Berkeley, CA 94720, USA*

(July 2, 2002)

Abstract

We demonstrate the application of surface sensitive diffuse x-ray scattering under the condition of grazing incidence and exit angles to investigate growth and dissolution of near surface defects after boron implantation in silicon (001) and annealing. Silicon wafers were implanted with a boron dose of 6×10^{15} ions/cm^2 at 32keV and went through different annealing treatments. From the diffuse intensity close to the (220) surface Bragg peak we reveal the nature and kinetic behavior of the implantation induced defects. Analyzing the q dependence of the diffuse scattering, we are able to distinguish

between point defect clusters and extrinsic stacking faults on {111} planes. Characteristic for stacking faults are diffuse x-ray intensity streaks along ⟨111⟩ directions which allow for the determination of their growth and dissolution kinetics. For the annealing conditions of our crystals, we conclude that the kinetics of growth can be described by an Ostwald ripening model in which smaller faults shrink at the expense of the larger stacking faults. The growth is found to be limited by the self diffusion of silicon interstitials. After longer RTA the stacking faults disappear almost completely without shrinking, most likely by transformation into perfect loops via a dislocation reaction. This model is confirmed by complementary cross-sectional transmission electron microscopy (TEM).

61.10.Eq, 61.72.-y

Typeset using REVTEX

I. INTRODUCTION

Ion implantation plays a central role in the production of integrated circuits in semiconductor technology and is by far the preferred doping technique for silicon wafers. An energetic ion impinging on the silicon lattice produces a cascade of displacements and defects before coming to rest in the crystal. These defects are mostly Frenkel pairs consisting of vacancies and interstitials that recombine in the very earliest stages of annealing. However, when the implanted boron occupies an electrically active substitutional site it must displace a silicon atom, which then becomes an interstitial atom. These interstitials form the basis of the +1 model.[1,2] The high supersaturation of these +1 interstitials drives a number of defect processes as the implanted crystal is subjected to thermal treatment. Point defects, defect clusters and dislocation loops are formed and can substantially influence the electronic properties. A typical example of such unwanted side effects is the phenomenon of transient enhanced diffusion (TED), in which (depending on the temperature) the diffusion of the dopant atoms can be orders of magnitude higher than for dopant atoms in an unimplanted silicon lattice.[2] While the interactions between the implanted ions and the lattice point defects, leading to such effects like TED, have been investigated extensively and are now considered to be reasonably well understood,[3] the formation and annihilation of larger defect structures such as stacking faults and {311} defects are still under discussion.[4]

From the experimental point of view the structural characterization of extended defects becomes even more difficult as their spatial dimensions reaches into the sub-micrometer range and thus are less suitable for scanning electron microscopy. In addition, the range of implantation energies, the implantation conditions and the thermal budget during post-implantation processing leads to a complex parameter field for the implantation related processes. For a reliable control of the semiconductor manufacturing process and for a fundamental understanding of the physics a detailed investigation of the defect properties and their diffusion behavior as a function of annealing time and temperature is therefore required.

In what follows, we demonstrate that surface sensitive x-ray methods using grazing incidence and exit angles are especially well suited for the investigation of near surface defects caused by implantation and annealing. These investigations are non-destructive and do not require any special sample preparation. In addition, with a typical mm-size x-ray beam a statistically large number of defects is sampled. For comparison, cross-sectional transmission electron microscopy (TEM) would require a huge number of samples to give statistically significant results. Using grazing incidence x-ray diffuse scattering in the Bragg tails (Huang scattering) Beck et al.[5] have demonstrated the presence of point defect clusters in boron implanted silicon. In addition a technique was developed which allowed for the detection of extrinsic stacking faults on $\{111\}$ planes. These defects produce narrow diffuse streaks of intensity along $\langle 111 \rangle$ directions.[5,6]

Starting from these findings, we report in this paper on the growth and dissolution of defect structures in boron implanted silicon as a function of annealing temperature and time. For this purpose, several sample series with systematically varying annealing temperatures and times were prepared. From our measurements we develop a model for the growth and dissolution kinetics, including the determination of the formation energy for the growth of extrinsic stacking faults. Atomic force microscopy (AFM) and cross-sectional transmission electron microscopy (TEM) are applied for the investigation of the surface and the crystalline structure of the samples and provide complementary confirmation of the kinetic model derived from the x-ray measurements.

II. SCATTERING UNDER GRAZING INCIDENCE

A. Bragg-diffraction

For incidence angles α_i close to the critical angle of total external reflection α_c, the transmitted x-ray wave is exponentially attenuated into the material with a characteristic penetration depth between a few tens and several hundred angstroms (so called "evanescent

wave"). The wave vector lies nearly parallel to the surface and is Bragg-diffracted by lattice planes perpendicular to the surface, finally leaving the crystal under a grazing exit angle α_f. In the distorted wave Born approximation[7] the scattered signal is governed by the structure factor $S(\vec{Q}')$ of the Bragg reflection and the transmission coefficients for incidence t_i and exit t_f:[8]

$$I_{GID}(\vec{Q}') \propto \mid t_i \mid^2 S(\vec{Q}') \mid t_f \mid^2 \tag{1}$$

The momentum transfer in z direction, perpendicular to the sample surface, is a complex quantity:[9]

$$Q'_z = k_f^{(z)'} - k_i^{(z)'} \tag{2}$$

with

$$k_{i,f}^{(z)'} = \pm \left(\frac{2\pi}{\lambda} \right) \sqrt{\sin^2 \alpha_{i,f} - 2\delta - i2\beta}. \tag{3}$$

By varying the angles α_i and α_f the method is depth sensitive. The scattered intensity stems from a scattering depth Λ:[8]

$$\Lambda = \frac{1}{\mid Im(Q'_z) \mid} \tag{4}$$

determined by α_i and α_f, the absorption β and dispersion δ of the index of refraction.

For the calculation of the structure factor in equation (1) the scattering vector $\vec{Q}$ is split into components parallel and perpendicular to the surface. The evaluation yields:[8]

$$S_{Bragg}(\vec{Q}_{\parallel}, Q'_z) = \mid F_{hkl} \mid^2 \delta(\vec{Q}_{\parallel} - \vec{G}_{hkl}) \frac{1}{\mid 1 - e^{iQ'_z a_\perp} \mid^2} \tag{5}$$

with the structure factor F_{hkl} of the unit cell, the lattice constant $a_\perp$ in growth direction and the associated reciprocal lattice vector $\vec{G}_{hkl}$.

For crystals with defects, diffuse scattering is expected close to Bragg reflections at $\delta(\vec{Q}_{\parallel} - \vec{G}_{hkl})$. For $\alpha_{i,f} < \alpha_c$ the increase of the diffuse intensity is governed by the transmission functions t_i and t_f, while above α_c the product of the diffuse structure factor and Λ leads to an almost constant intensity distribution along Q'_z.

B. Scattering from crystals with defects

In general, point-defects in a crystalline lattice induce a displacement field which in the elastic limit decreases with $1/r^2$, where r is the distance from the defect. Depending on the nature of the defect the mean lattice constant is changed and the deviation $\vec{s}_m$ of the lattice atoms (m) from their ideal position $\vec{r}_m$ induces diffuse x-ray scattering, especially close to the Bragg peaks, accompanied by an intensity reduction of the Bragg reflections.[10]

1. Diffuse scattering due to point defects

The point defect induced diffuse scattering at an arbitrary position in reciprocal space can be written as:

$$I_{diff}(\vec{Q}) = I(\vec{Q}) - I_{Bragg}(\vec{Q}). \tag{6}$$

If the defects are not correlated and the displacement of an atom is given by the linear superposition of the distortions from single defects, the diffuse intensity can be calculated in kinematic approximation for the case of small displacements:[10,11]

$$I_{diff}(\vec{Q}) = c \ \mid f_D(\vec{Q}) + \sum_m f_m e^{i\vec{Q}\cdot\vec{r}_m} \left(e^{i\vec{Q}\cdot\vec{s}_m} - 1\right) \mid^2. \tag{7}$$

c indicates the defect concentration, f_D is the scattering contribution due to the defect itself, while the summation describes the diffuse scattering amplitude f from the lattice atoms m displaced from their ideal positions $\vec{r}_m$ by $\vec{s}_m$ due to the presence of the defects. This second contribution represents the major part of the diffuse scattering and is usually divided in different contributions depending on the appropriate approximations in the description of the scattering. For small enough displacements and for large r, the exponential in Eq. (7) can be expanded and reduced to the linear term. Neglecting the Laue term $f_D(\vec{Q})$ and with $\vec{Q} = \vec{G} + \vec{q}$ the diffuse intensity can be calculated as:[12]

$$I_{diff}(\vec{Q}) \propto \langle \mid A(\vec{Q}) \mid^2 \rangle \tag{8}$$

$$\approx \langle\left(\mid \vec{G}\cdot\vec{s}(\vec{q}) \mid^2 -2\,i\,\vec{G}\cdot\vec{s}(\vec{q})\,L\right)\rangle e^{-2L},$$

where $\vec{s}(\vec{q})$ is the fourier transform of the displacement field and the average is taken over all possible defect configurations in the lattice. L designates the static Debye Waller factor. The first symmetric term is proportional to $1/q^2$ and the second expression is proportional to $1/q$.

2. Diffuse scattering from defect clusters

A cluster is usually described as a point defect composed of n single defects. Assuming again a linear superposition of the long-range displacement field of the single defects in the cluster, the diffuse intensity, induced by a cluster concentration c is:[10]

$$I_{diff}^{Cluster} = \frac{c}{n} \mid nA^{single} \mid^2 = n \; I_{diff}^{single}. \tag{9}$$

The diffuse intensity increases by a factor n, caused by the coherent addition of the scattering amplitudes from the single defects within the cluster. This represents the Huang scattering limit for the diffuse scattering from clusters and is only valid as long as the total displacements around the cluster is small enough to allow for the above mentioned expansion of the exponential term in Eq. (7). The corresponding distance R_{cl} (for "small" enough displacements) is defined as the cluster radius. Stronger displacements for $r < R_{cl}$ have to be treated in the so called Stokes-Wilson approximation[13] leading to the expression:

$$I_{diff} \propto c\frac{G}{q^4}. \tag{10}$$

The crossover from the Stokes-Wilson-Scattering to the Huang-scattering region in reciprocal space i. e. the crossover between the q^{-4}- and the q^{-2}-decay of the diffuse intensity can be exploited to determine the "size" R_{cl} of the clusters from the simple relationship $q = 1/R_{cl}$.

It should be pointed out that the displacements due to vacancies are much smaller than for interstitial point defects and their clusters. The associated diffuse scattering being proportional to the square of the Fourier transform of the displacement field is thus rather insensitive to the presence of vacancies.

7

Dislocations and stacking faults are large defects often found in semiconductors especially as a result of ion implantation and annealing. In general they induce distortions and thus diffuse scattering.[14]

The strength and orientation of a dislocation is described by its Burgers vector $\vec{b}$, which in general is a lattice vector of the crystal matrix. Such dislocations are called "perfect dislocations". A Burgers vector not fulfilling this condition characterizes a "partial dislocation", which is only stable in certain lattice types and for certain dislocation orientations. An example for these non-perfect dislocations are stacking faults in fcc and diamond lattices. They are formed when the stacking sequence $(\ldots ABCABCABC \ldots)$ of the (111) planes is disrupted in $\langle 111 \rangle$ direction, where A, B and C denote double planes in the case of the diamond lattice. Thereby, large planar defects can be formed with closed partial dislocations at their boundaries. Stacking faults can be *intrinsic (ISF)* or *extrinsic (ESF)*.

ISF are formed when an atomic layer is removed from the stacking sequence, whereas for ESF an additional layer is inserted into the lattice. Both can be bound by Frank partial dislocation loops, which have a Burgers vector $\vec{b} = \frac{a}{3} \langle 111 \rangle$ with the lattice constant a. The investigated boron implanted silicon samples show stacking faults of the extrinsic type.[5]

The theory of diffuse scattering caused by stacking faults and dislocation loops[15,16] predicts in the case of extrinsic stacking faults on $\{111\}$ planes:

1. Diffuse intensity streaks in the $\langle 111 \rangle$ directions of the Burgers vector of the Frank loop.

2. Constant width of the streaks along the Burgers vector direction.

3. $I_{diff} \propto q_{\langle 111 \rangle}^{-2}$ dependence along the $\langle 111 \rangle$ directions (Huang scattering).

As Larson et al.[15] have shown the scattering cross-section in the Huang approximation is given as the product of the Fourier transform $s(\vec{q})$ of the long range elastic displacement field $\vec{s}(\vec{r}) \parallel \vec{s}(\vec{q}) \parallel \vec{b}$ and the shapefunction sf of the stacking faults:

8

$$I_{HDS} \propto conc \; \text{sf}^2 \left[\vec{Q} \; \vec{s}(\vec{q}) \right]^2 \tag{11}$$

For disk-shaped extrinsic stacking faults with a radius R_{SF} the shape function can be approximated by an expression including a Bessel function J_1:[15]

$$\text{sf} = 2 \frac{J_1(QR_{SF})}{QR_{SF})} \tag{12}$$

Q describes the projection of $\vec{q}$ in the (111) plane. The Huang scattering induced by extrinsic stacking faults on $\{111\}$ planes can therefore be described by

$$I_{HDS} \propto conc \times \left(2 \frac{J_1(QR_{SF})}{QR_{SF})} \right)^2 \times \left(\frac{Q}{q} \right)^2 \times \frac{\vec{b}}{|\vec{b}|} \tag{13}$$

III. EXPERIMENTAL DETAILS

The starting material for the samples analyzed in this work consist of dislocation free, floating-zone silicon (001) single crystals. They were cleaned and implanted with a high boron dose of 6×10^{15} ions/cm^2 at 32keV. Following implantation the samples were annealed for 15min at 750°C in a furnace under UHV conditions. Thereafter the samples went through rapid thermal annealing (RTA) in an argon atmosphere for various times between 10sec and 160sec in a temperature range between 900°C and 1060°C. Another sample series was studied which was implanted with a boron dose of 5×10^{15} ions/cm^2, but treated by RTA only for times between 10 sec and 240sec at a temperature of 975°C. Details of the sample preparation are listed in table I.

At the implantation energy of 32keV, the maximum of the boron concentration is at 120nm and the damage distribution extends to about 350nm below the crystal surface (see Fig. 11). To attain near surface sensitivity and suppress bulk scattering all measurements of diffuse x-ray scattering were done in the geometry of grazing incidence and grazing exit[17] as shown in Fig. 1. The diffracting planes in this case are normal to the (001) crystal surface. The incident angle α_i was set to 0.35° which corresponds to a penetration depth of about $1\mu m$ at an x-ray energy of 9keV. For efficient data collection along the exit angle a linear

9

position sensitive detector (PSD) was mounted perpendicular to the (001) sample surface. This scattering geometry restricts the diffraction volume significantly and thus mandates the use of synchrotron radiation.

The diffuse scattering was also measured under the same conditions of pure untreated floating zone silicon. Subtracting the thermal diffuse scattering of the pure silicon from all measurements of the implanted samples allows for the determination of the pure defect induced scattering intensity. Three dimensional reciprocal space maps were recorded in the vicinity of the (220) surface Bragg reflection in transverse [$1\bar{1}0$] and longitudinal [110] directions as shown in Fig. 2.

The defect induced diffuse intensity in the transverse scans is mainly due to point defects and point defect clusters (see later). The scans in longitudinal direction, showing strong diffuse intensity streaks along $\langle 111 \rangle$ directions, were analyzed using the theory of diffuse scattering from stacking faults (see Sec. II B 3). Since the surface could also act as a sink for defects generated by implantation, we employed atomic force microscopy (AFM) to study changes in surface morphology after annealing. Transmission electron microscopy (TEM) was also employed to determine the nature and spatial distribution of defects in the implanted layer.

IV. RESULTS

A. Diffuse scattering in transverse direction

The intensity distribution of the reciprocal space maps recorded in transverse direction around the (220) surface Bragg reflection ((110) plane) are shown in Fig. 3. The defect induced diffuse scattering integrated along the PSD in q_z direction is plotted as a function of q_{trans} through the (220) reciprocal lattice point on a double logarithmic scale. We find the characteristic q dependence of strongly distorting defect clusters as described in Sec. II. For small q the Huang approximation of diffuse scattering from point defects (q^{-2} dependence)

is still valid. For larger q values a q^{-4} dependence is observed (Stokes-Wilson scattering). From the crossover of the slope at q_{cr} the defect cluster radius R_{cl} is determined using the relation $q_{cr}R_{cl} = 1$. Though the results in Fig. 3 seem to indicate that the cross-over point occurs at larger q_{trans} (decreasing cluster size) with increasing time, we feel that the shift is within the experimental uncertainty of the measurements. Therefore we assign an average cluster radius of (20 ± 5)Å to our findings. This cluster radius is independent of the RTA time and temperature as we find the same q_{cr} for all investigated samples. In order to capture the dissolution of the clusters, the diffuse scattering intensity integrated from $0.5\text{nm}^{-1} \leq q_{trans} \leq 1.0\text{nm}^{-1}$ (q^{-4} range) is shown in Fig. 4 as a function of the annealing time for different temperature treatments. While the q dependence of the diffuse intensity remains the same for all annealing treatments, the level of diffuse scattering decreases substantially with longer annealing times.

We associate the cluster with a remarkably stable B_3I configuration consisting of three boron atoms and one interstitial, which has been postulated from recent first principles studies of boron clustering in the presence of excess self interstitial atoms.[18] As pointed out earlier (see Sec. IIB2) the cluster radius R_{cl} as obtained from the q dependence of the diffuse scattering is expected to be larger than the actual physical cluster size. This explains the observed cluster diameter being larger than expected for B_3I.

The samples without furnace annealing show a 2.5 times smaller initial number of defect clusters. The observed cluster radius however remains the same. This is to be expected, since annealing of defects is faster and more effective at higher temperatures while the clusters formed at 750°C with a higher supersaturation of interstitial atoms, will take longer to dissolve.

B. Diffuse scattering in longitudinal direction

The main feature of the intensity distribution in the $(1\bar{1}0)$ plane (q_{long}-q_z mapping) is the observation of diffuse intensity streaks along $\langle 111 \rangle$ directions, which dominate the measured

intensity (see Fig. 5(a)). These streaks have been shown to be due to extrinsic stacking faults on {111} planes bounded by Frank loops with Burgers vector $\vec{b} = \frac{a}{3}(111)$, as they show all three characteristic features predicted by theory: 1) Diffuse intensity streaks occur in the $\langle 111 \rangle$ directions of the Burgers vector. 2) The half-width of the streaks perpendicular to the [111] direction remains essentially constant along the streak (see Fig. 6). 3) The integrated streak intensity obeys the $q_{\langle 111 \rangle}^{-2}$ law (see Fig. 7).

For the sample series annealed at 1060°C RTA, the intensity of diffuse scattering in the q_{long} - q_z plane for different annealing times is shown in Fig. 8. The intensity of the $\langle 111 \rangle$ streaks initially increases with annealing time, reaches a maximum and subsequently decreases. For sufficient long times the streaks vanish almost completely.

Using Eq. (13) to fit the intensity slice perpendicular to the streaks at any $q_{\langle 111 \rangle}$ (see Fig. 6) we find the average radius of the stacking faults from the half-width (FWHM). The total number of silicon interstitials bound to stacking faults is deduced from the integrated intensity of the streaks. Both quantities are obtained as a function of the annealing time at a constant RTA temperature.

The half-width was determined in two ways. First along the q_z direction from the data directly measured with the PSD at the reciprocal lattice point (2.1 2.1 0.1) (see Fig. 5(b)) and second perpendicular to this direction using the transverse scan across the same reciprocal lattice position. After consideration of several corrections due to the scattering geometry and resolution effects, the streak half-width turns out to be the same in both directions. We conclude that the stacking faults are circular in shape. This has been confirmed by TEM micrographs.

Because measuring the width along the q_z direction required fewer corrections, the real-space diameter $d = 2\pi/FWHM$ used for further evaluation was determined using this method. The results are shown in Fig. 9(a) where the stacking fault diameter is depicted as a function of the annealing time. For all sample series we observe an immediate growth of the diameter with the beginning of the RTA treatment. For longer annealing times this growth saturates at a diameter of about 1000Å. Comparing different sample series we find, that the

growth process is faster at 1060°C than for sample series annealed at lower temperatures. Comparing the samples with pre-annealing (b1c series) and those with RTA treatment only (series b975) the pre-annealed samples show a slower growth process at comparable RTA temperatures. This is to be expected, since the pre-annealing at 750°C for 15min gives a drastic reduction in the supersaturation of interstitials introduced by implantation, leaving fewer interstitials available to contribute to any stacking fault growth.

In Fig. 9(b) the integrated intensity of the streaks at (2.1 2.1 0.1) versus the RTA time is shown for the same sample set. For all series we observe a decrease of the intensity for longer annealing times. In a manner similar to the kinetics of growth of the stacking fault diameter, the decrease and the complete vanishing of the integrated streak intensity happens much faster at higher RTA temperatures. In particular it is remarkable that at the same time as the integrated streak intensity and thus the total number of silicon interstitials in stacking faults vanishes the stacking fault diameter keeps growing or at least remains constant. This effect can be observed for all sample series. It means that the disappearance of the stacking faults is not caused by their shrinking but by their vanishing as a whole. This can occur through a dislocation reaction mechanism involving the nucleation of a Shockley partial sweeping through the stacking fault, leaving behind a perfect loop.[19]

C. Atomic force microscopy

The surface morphology of the samples as a function of the annealing treatment was studied by AFM on different length scales. As an example AFM images of $500nm \times 500nm$ size of the series annealed at 1060°C are shown in Fig. 10. Initially we observe a surface with an average roughness of about 0.15nm as shown in Fig. 10(a). For the sample which was RTA treated for 120sec at 1060°C (see Fig. 10(b)) nano-sized surface structures appear with an average height of 4nm. Since the initial wafer surfaces are flat and smooth, we attribute the features observed by AFM to be primarily due to those interstitial atoms, mainly silicon, that migrate during the early annealing stage from near surface regions in

13

the crystal. Subsequent, during longer annealing times a coarsening of the nano-features on the surface is observed.

Specular x-ray small angle reflectivity measurements show an increasing surface roughness for the sample series which were RTA treated at 1060°C for more than 40sec, which confirms the conclusion from the AFM measurements.

D. Transmission electron microscopy

In Fig. 11(a),(b) cross-section TEM micrographs of the samples, furnace annealed at 750°C for 15min, and additionally RTA treated at 1060°C for 10sec and 120sec are shown. After 10sec RTA (see Fig. 11(a)) we observe a layer of defect clusters and small dislocation loops, as well as a few large extrinsic stacking faults. On weak beam TEM images of [110] cross-sections these extrinsic stacking faults on {111} planes can be either observed on edge as inclined straight lines (($\bar{1}11$) and ($1\bar{1}1$) SFs) or as domains showing characteristic fringes due to the superposition of two translated domains ((111) and ($11\bar{1}$) SFs).

After 120sec RTA (see Fig. 11(b)) the image looks very different: all the defect clusters and extrinsic stacking faults have dissolved. Only a network of dislocation loops can be observed. This is consistent with our observation (see Fig. 9(b)) that the integrated streak intensity has vanished, since perfect loops do not give rise to streaks. We feel that these results strengthen our arguments for the dislocation reaction mechanism to account for the disappearance of stacking faults.[19]

V. DISCUSSION

From our measurements we propose a model for the growth and dissolution of defect structures in boron implanted silicon as a function of annealing temperature and time. Within this model the activation energy for the growth of extrinsic stacking faults is determined.

14

A. Model for defect evolution during annealing

The boron implantation induces a high supersaturation of silicon self-interstitials. Simulations using the TSUPREM4 code[20] show that, at very short annealing times (1-5sec), interstitials originating in the crystal layer between the surface and the maximum of the implant dose diffuse rapidly to the surface and cause the surface features we have reported earlier. The interstitials in the region of the maximum concentration of boron (about 120nm from the surface) are either trapped in boron clusters of the type referred to in Sec. IV A and Fig. 3, or give rise to extended defects at relatively low anneal temperatures (650-850°C). These extended defects are of the {311} type. Besides dissolving and providing interstitials for TED, some of them evolve into Frank partial dislocation loops which are, in addition to the immobile clusters, the primary defects observed in the temperature range 900-1100°C.

Initially, the stacking faults grow in size by capturing free silicon interstitials that are left over from the pretreatment at 750°C. In this phase we observe growth of both the integrated streak intensity (i.e. the number of silicon interstitials bound in stacking faults) and also the stacking fault diameter. For the investigated sample series this happens during the first seconds of RTA treatment (< 10sec). The stacking faults have a circular shape. Their extrinsic character is demonstrated by the displacement field induced asymmetry of the streaks in [$\bar{1}\bar{1}1$] and [111] direction.[16,21,22]

Depending on the RTA temperature the integrated streak intensity reaches a maximum and remains constant typically after a few seconds only. During subsequent annealing times the total number of silicon interstitials in stacking faults stays the same while the diameter of the faults keeps on growing (see Figs. 9(b) and 9(a)). The effect is observed for all investigated sample series. This process where the larger precipitates grow at the expense of the smaller ones is characteristic for conservative Ostwald ripening.[23] The chemical potential of silicon atoms around dislocation loops of different sizes provides the driving force for the coarsening.[24] It results in a reduction of the total interfacial and elastic energy. The stacking faults keep on growing up to a maximum radius of about 1000Å. The existence of a largest

radius was explained by calculations of the stability of extrinsic stacking faults (i.e. faulted Frank dislocation loops) versus perfect dislocation loops by Cristiano et al.[4] They find, in good agreement with our measurements, that for a diameter larger than 1000Å the stacking faults on {111} planes are no longer the most stable configuration.

For longer annealing times (about 20sec for the series b1c1060, much longer for lower RTA temperatures) the integrated streak intensity decreases, while the diameter of the faults remains constant (see Figs. 9(b) and 9(a)). We conclude that the stacking faults disappear without a shrinking process. This result can be explained by a dislocation reaction mechanism as pointed out earlier and can be expressed as $1/3(111) + 1/6(11\bar{2}) \rightarrow 1/2(110)$. In this reaction the energy of the dislocations involved is the same on either side of the reaction; however, the net energy is lowered by the removal of the stacking fault. This is also consistent with the experimental observation that the fault configuration is unstable as the loop diameter exceeds a certain size (approx. 1000Å).

This mechanism is supported by the TEM measurements (see Fig. 11). Using TEM we observe that after 120sec RTA at 1060°C, most of the faulted Frank dislocations deep in the substrate have transformed into perfect loops. At the same time the integrated streak intensity has already almost vanished.

B. Activation energy for the formation of stacking faults

Based on the model of the defect evolution during the annealing process presented in the previous chapter, especially taking into account the conservative Ostwald ripening model, we determine the formation energy for the growth of extrinsic stacking faults. For the calculation we use an approach which was developed by Bonafos et al.[24] for a similar sample system. They start from a theory based on Ostwald ripening,[23] which was adapted to the particular geometry of dislocation loops (Burton and Speight's model[25]).

Bonafos et al.[24] showed that simple analytic laws can describe the process, after the steady-state growth stage is reached, i.e. when the growth consists in an exchange of atoms

between the loops of a constant interstitial population. In this case the loop density varies with $1/t$ while the mean radius increases with $t^{0.5}$. t designates the annealing time. The activation energy E_{act} can be determined from[24]

$$T\bar{r}^2 exp\left(\frac{-a}{\bar{r}}\right) = Cexp\left(\frac{-E_{act}}{kT}\right) \qquad (14)$$

with annealing temperature T, average stacking fault radius $\bar{r}$ and two constants a and C.

The time dependence of the loop density and the mean radius is shown in Figs. 12(a) and 12(b). The prerequisites for the Bonafos approach are fulfilled as long as we can assume conservative Ostwald ripening. Having proved the applicability of this approach from the time dependence of Fig. 12 we determine the formation energy from Fig. 13 using Eq. (14). We find an average activation energy for the growth of the extrinsic stacking faults on $\{111\}$ planes of about 4.4eV ($\pm 10\%$). Within the statistical uncertainty this value is consistent with the value for self-diffusion of silicon atoms of (4.75 ± 0.04)eV.[26] From these results we conclude that once an extrinsic stacking fault has been formed the subsequent growth of the stacking fault is limited by the diffusion of the silicon interstitials.

VI. CONCLUSION

Summarizing, we have systematically investigated defect structures in silicon which was implanted with a high boron dose and subsequently annealed at low temperature and by a rapid thermal process. We demonstrate that diffuse x-ray scattering at grazing incidence and exit angles is well suited to quantitatively investigate near-surface defects. The method is sensitive to exactly the depth in which the defects are located ($\ll 1\mu m$). As compared to TEM the technique is non-destructive and the buried defect structures can be investigated without any special sample preparation. The integration over a macroscopic scattering volume provides a good statistical averaging, whereas for TEM and AFM only a small fraction of the sample is accessible.

From the q dependence of the diffuse intensity different defect types (single defects, clusters, stacking faults) can be distinguished. Quantitative information about size and

17

density of the stacking faults can be achieved. A discrimination between intrinsic and extrinsic defects is possible as well. From our measurements we have developed a kinetic model for the growth and dissolution of defect structures in silicon. As AFM and TEM show a direct image of the surface morphology and the crystalline structure of the sample, these techniques were used to supplement the x-ray data.

Further studies revealing the depth distribution of the different kinds of defects from the α_i dependence of the diffuse scattering are currently under way. These results are especially interesting for ultra-low energy implantation for future Si based devices on the nano-scale.

ACKNOWLEDGMENTS

REFERENCES

[1] M. D. Giles, Appl. Phys. Lett. **62**, 1940 (1993).

[2] P. A. Stolk, H.-J. Gossmann, D. J. Eaglesham. D. C. Jacobson, C. S. Rafferty, G. H. Gilmer, M. Jaraiz, J. M. Poate, H. S. Luftman, and T. E. Haynes, J. Appl. Phys. **81**, 6031 (1997).

[3] E. Chason, S. T. Picraux, J. M. Poate, J. O. Borland, M. I. Current, T. Diaz de la Rubia, D. J. Eaglesham, O. W. Holland, M. E. Law, C. W. Magee, J. W. Mayer, J. Melngailis, and A. F. Tasch, J. Appl. Phys. **81**, 6513 (1997).

[4] F. Cristiano, J. Grisolia, B. Colombeau, M. Omri, B. de Mauduit, A. Claverie, L. F. Giles, and N. E. B. Cowern, J. Appl. Phys. **87**, 8420 (2000).

[5] U. Beck, T. H. Metzger, J. Peisl, and J. R. Patel, Appl. Phys. Lett. **76**, 2698 (2000).

[6] I. Kegel, M. Sztucki, T. H. Metzger, D. Lübbert, J. Arthur, and J. R. Patel, Mat. Res. Soc. Symp. Vol. **610**, B5.5.1 (2000).

[7] G. H. Vineyard, Phys. Rev. B **26**, 4146 (1982).

[8] H. Dosch, Critical Phenomena at Surfaces and Interfaces - Evanescent X-ray and Neutron Scattering, (Springer, Berlin, 1992).

[9] H. Dosch, Phys. Rev. B **35**, 2137 (1987).

[10] P. Ehrhart, J. Nucl. Mater. **216**, 170 (1994).

[11] P. H. Dederichs, J. Phys. F: Metal Physics **3**, 471 (1973).

[12] B. C. Larson, and W. Schmatz, Phys. Rev. B **10**, 2307 (1974).

[13] H. Trinkaus, Z. Naturforsch. **28a**, 980 (1973).

[14] H. Trinkaus, Phys. Status Solidi B **54**, 209 (1972).

[15] B. C. Larson, and W. Schmatz, Phys. Status Solidi B **99**, 267 (1980).

[16] K. Nordlund, U. Beck, T. H. Metzger, and J. R. Patel, Appl. Phys. Lett. **76**, 846 (2000).

[17] S. Grotehans, G. Wallner, E. Burkel, H. Metzger, J. Peisl, and H. Wagner, Phys. Rev. B **39**, 8450 (1989).

[18] T. J. Lenosky, B. Sadigh, S. K. Theiss, M-J. Caturla, and T. Diaz de la Rubia, Appl. Phys. Lett. **77**, 1834 (2000).

[19] F. R. N. Nabarro, Dislocations in solids, volume 2 (North-Holland, Amsterdam, 1979), Ch. 6.

[20] TSUPREM4 is a commercial version of the Stanford University program SUPREM4 originally written at Stanford University by M. E. Law, C. S. Rafferty, and R.W. Dutton.

[21] K. Nordlund, P. Partyka, R. S. Averback, I. K. Robinson, and P. Ehrhart, J. Appl. Phys. **88**, 2278 (2000).

[22] P. Ehrhart, H. Trinkaus, and B. C. Larson, Phys. Rev. B **25**, 834 (1982).

[23] W. Ostwald, Z. Phys. Chem. **34**, 495 (1900).

[24] C. Bonafos, D. Mathiot, and A. Claverie, J. Appl. Phys. **83**, 3008 (1998).

[25] B. Burton, and M. V. Speight, Philos. Mag. A **53**, 385 (1985).

[26] H. Bracht, E. E. Haller, and R. Clark-Phelps, Phys. Rev. Lett. **81**, 393 (1998).

TABLES

TABLE I. List of investigated Si samples

series	B implantation [ions/cm^2]	furnace annealing T, time	RTA annealing T, time range
b1c1060	6×10^{15}	750°C, 15 min	1060°C, 10 - 120 sec
b1c1000	6×10^{15}	750°C, 15 min	1000°C, 10 - 160 sec
b1c950	6×10^{15}	750°C, 15 min	950°C, 10 - 160 sec
b1c900	6×10^{15}	750°C, 15 min	900°C, 10 - 160 sec
b975	5×10^{15}		975°C, 10 - 240 sec

FIGURES

FIG. 1. Geometry used to measure the diffuse x-ray scattering under grazing incidence and exit. The diffuse scattering is measured by a linear position sensitive detector (PSD) mounted perpendicular to the sample surface.

FIG. 2. Three dimensional reciprocal space maps were recorded in the vicinity of the (220) surface Bragg reflection by performing transverse and longitudinal scans using a PSD to measure the intensity along the q_z direction.

FIG. 3. Defect cluster induced diffuse scattering integrated in q_z direction as a function of q_{trans}: from the slope crossover the cluster radius R_{cl} is determined. The trend of the crossover to larger q is not significant. The error bar has been determined by averaging over many other measurements not shown here.

FIG. 4. Diffuse scattering intensity in transverse direction as a function of annealing time indicating the remaining number of clusters. Measurements are shown for two sample series with pre-annealing in a furnace and RTA at 1060°C or 950°C and for the series treated by RTA at 975°C only.

FIG. 5. (a) Diffuse intensity streaks along $\langle 111 \rangle$ directions in a q_{long}-q_z intensity map close to the (220) surface reflection. These streaks are induced by extrinsic stacking faults on {111} planes. (b) Intensity distribution in q_z direction as measured by the PSD (vertical bar in (a)). The data were fitted with a Lorentzian function.

FIG. 6. The FWHM of the streaks induced by stacking faults on {111} planes remains essentially constant along the Burgers vector direction $\langle 111 \rangle$.

FIG. 7. The integrated intensity of the streaks as a function of $q_{\langle 111 \rangle}$ shows the q^{-2} behavior characteristic for Huang scattering. The diffuse scattering is integrated along the q_z direction as shown by the vertical bar in Fig. 5(a).

FIG. 8. Diffuse scattering in the q_{long} - q_z plane for different annealing times at a RTA temperature of 1060°C. The intensity of the streaks initially increases with annealing time, reaches a maximum and subsequently decreases. For sufficiently long times the streaks vanish almost completely.

FIG. 9. Stacking fault diameter (a) and integrated intensity of the streaks (b) as a function of the annealing time for samples annealed at temperatures indicated in the legend.

FIG. 10. AFM image of the sample surface annealed at 1060°C for 10sec (a) and 120sec (b). Nano-sized surface structures with an average height of 4nm appear after an annealing time of 120sec.

FIG. 11. Cross-section TEM image of the sample annealed at 1060°C for 10sec (a) and 120sec (b). Extrinsic stacking faults (in (a)) disappear most likely by transformation into perfect loops via a dislocation reaction mechanism.

FIG. 12. Variation of the inverse of the loop density (a) and variation of the square of the stacking fault radius (b) as a function of annealing time for two different RTA temperatures. The condition for a linear dependance is fulfilled as indicated by the straight lines in both cases. For the series b1c1060 and annealing times larger than 20sec we do not expect conservative Ostwald ripening, as the integrated streak intensity (see Fig. 9(b)) is no longer constant.

FIG. 13. Determination of the activation energy for the formation of stacking faults using Eq. (14) (according to Bonafos et al.[24]).
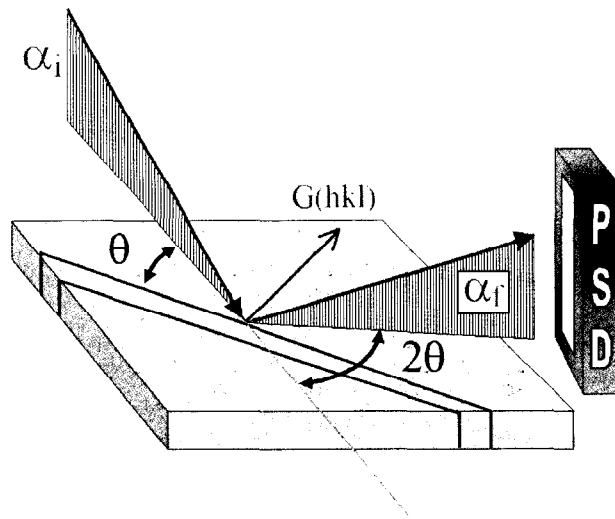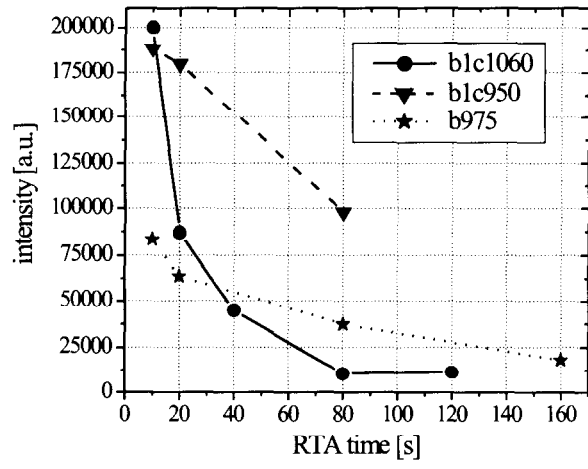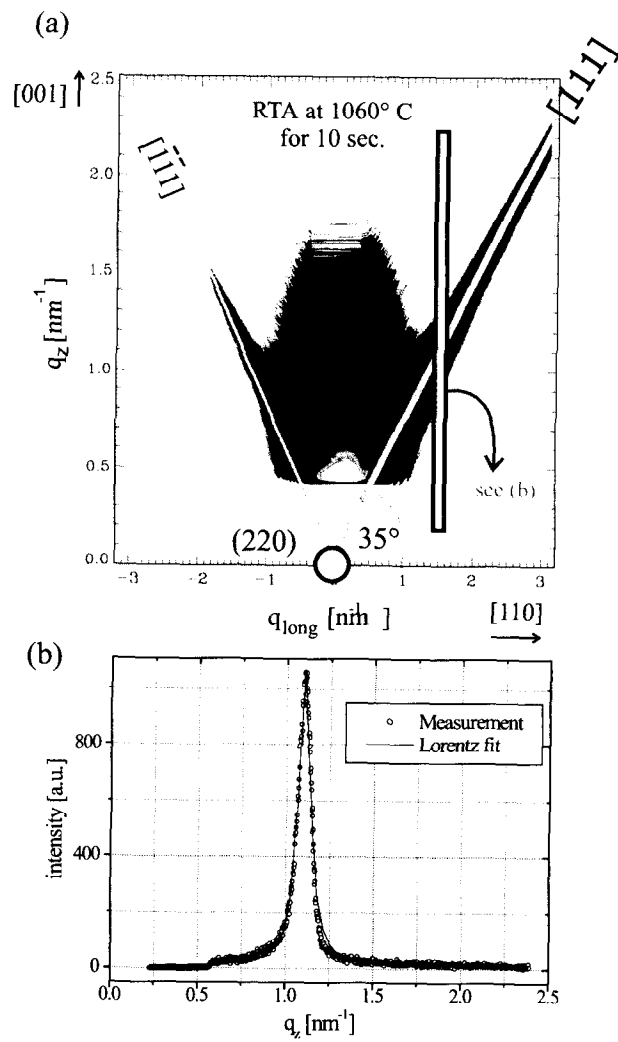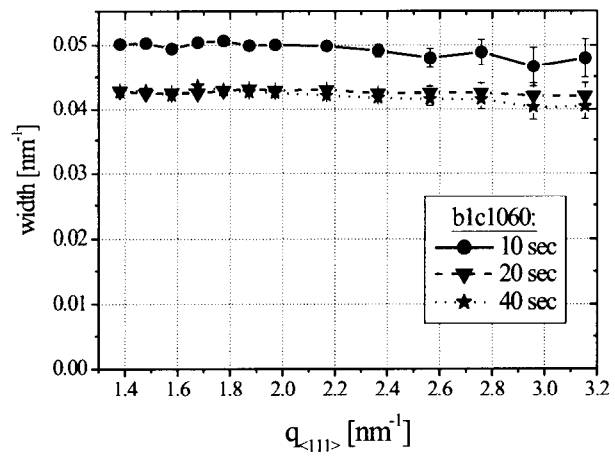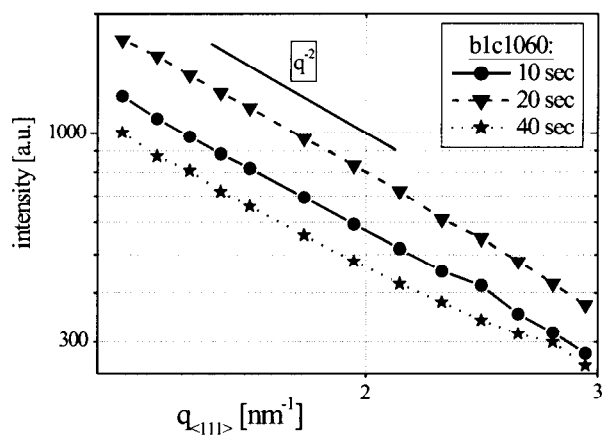
FIG. 1.

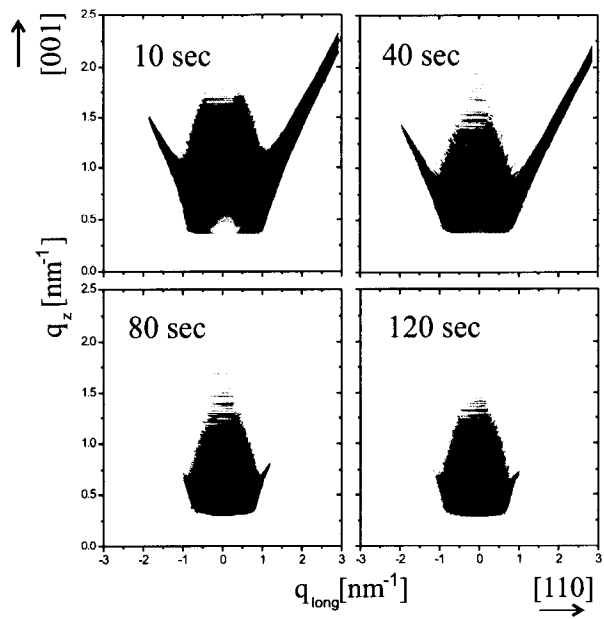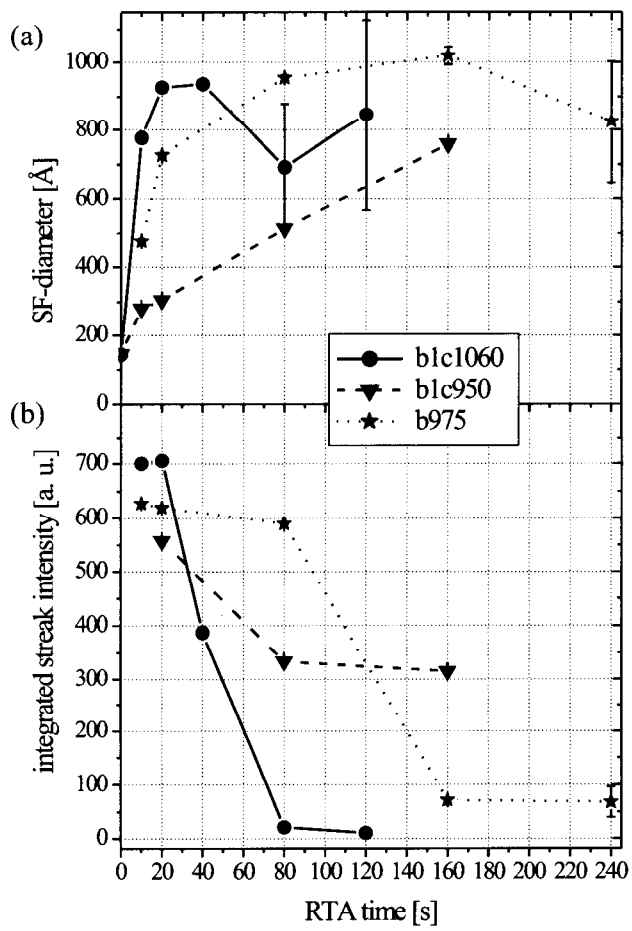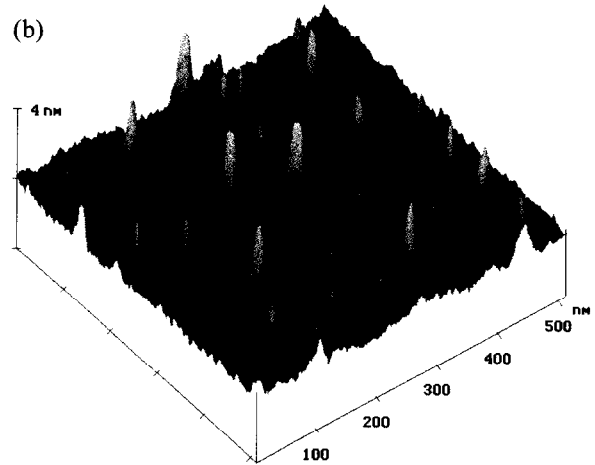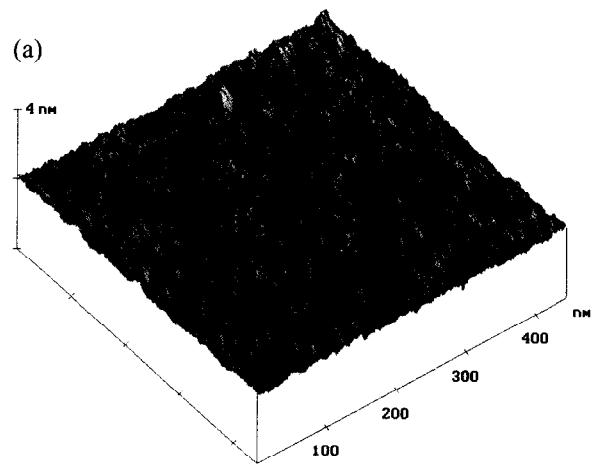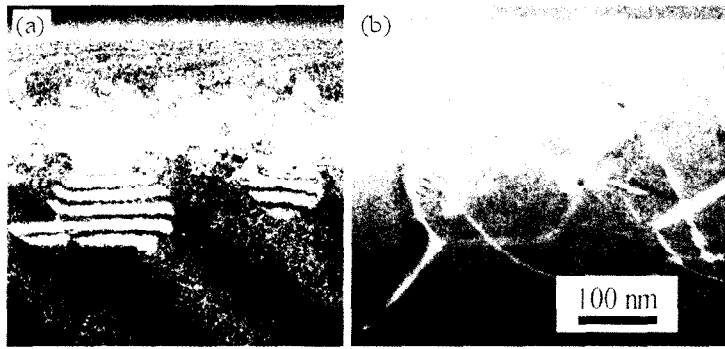M. Sztucki

J. Appl. Phys.
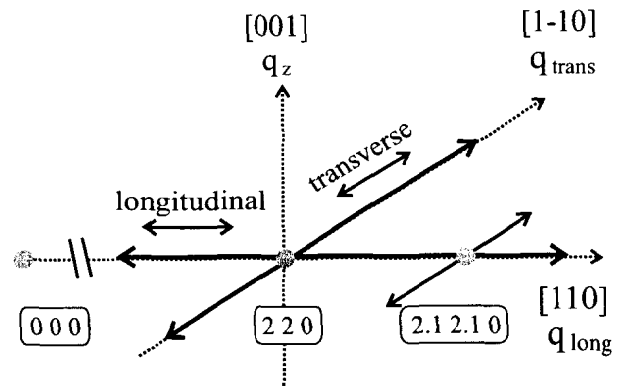
FIG. 2.

M. Sztucki

J. Appl. Phys.
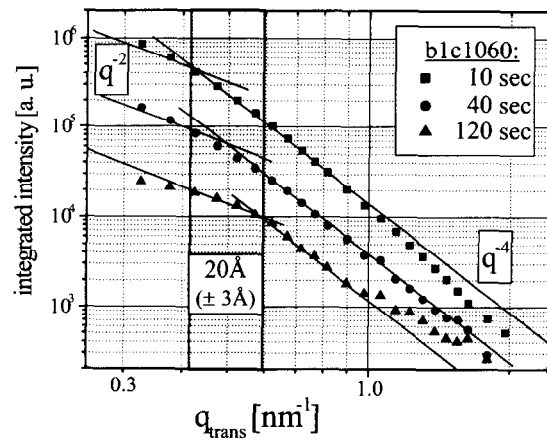
FIG. 3.

M. Sztucki

J. Appl. Phys.

FIG. 4.

M. Sztucki

J. Appl. Phys.

(a)

[001]

RTA at 1060° C
for 10 sec.

q_z [nm^{-1}]

$[\bar{1}\bar{1}1]$

$[111]$

see (b)

(220)   35°

q_{long} [nm]   [110]

(b)

intensity [a.u.]

o   Measurement
——— Lorentz fit

q_z [nm^{-1}]

FIG. 5.

M. Sztucki

J. Appl. Phys.

28

FIG. 6.

M. Sztucki

J. Appl. Phys.

FIG. 7.

M. Sztucki

J. Appl. Phys.

FIG. 8.

M. Sztucki

J. Appl. Phys.

FIG. 9.

M. Sztucki

J. Appl. Phys.

32

(a)

4 nm

nm

400

300

200

100

(b)

4 nm

nm

500

400

300

200

100

FIG. 10.

M. Sztucki

J. Appl. Phys.

33

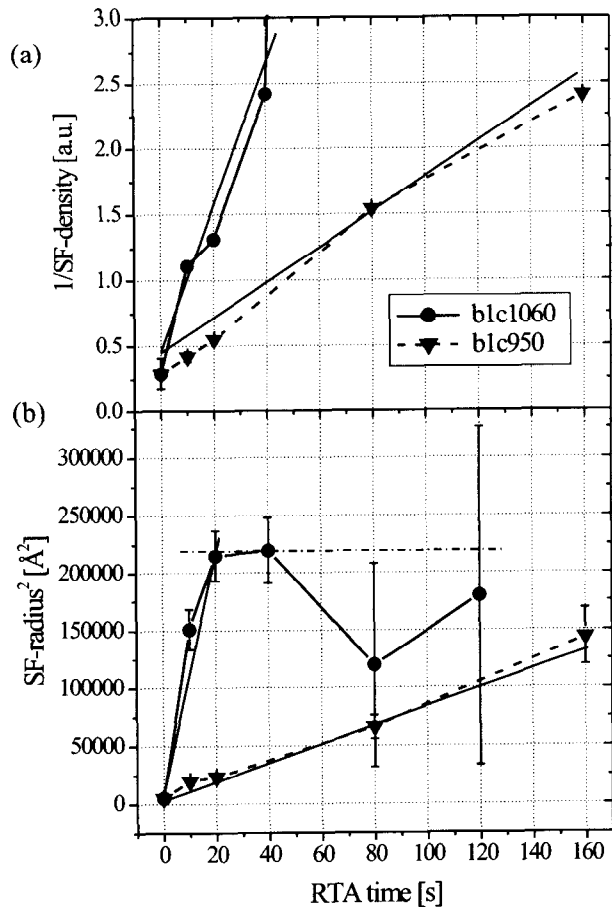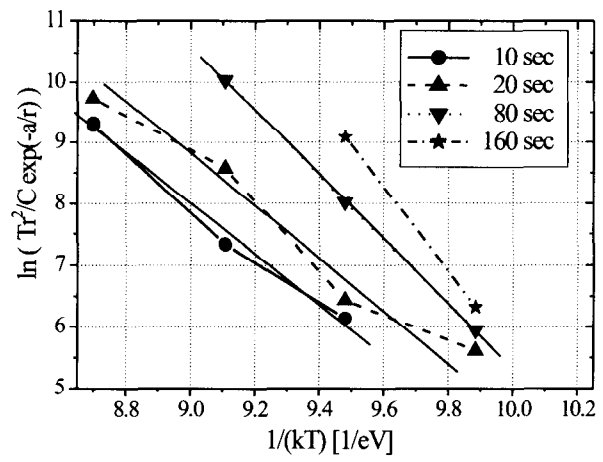(a) (b)

100 nm

FIG. 11.

M. Sztucki

J. Appl. Phys.

FIG. 12.

M. Sztucki

J. Appl. Phys.

FIG. 13.

M. Sztucki

J. Appl. Phys.